J Solid State Electrochem (2012) 16:2159–2167
DOI 10.1007/s10008-011-1628-9

ORIGINAL PAPER

The electrochemical properties of Al–Si–Ni alloys composed of nanocrystal and metallic glass for lithium-ion battery anodes

Linping Zhang · Xiaoping Song · Fei Wang · Qing Hu · Zhanbo Sun · Sen Yang · Liqun Wang · Shaodong Sun

Received: 7 November 2011 / Revised: 13 December 2011 / Accepted: 18 December 2011 / Published online: 12 January 2012

Abstract Melt-spun $Al_{75-X}Si_{25}Ni_X$ (X=2, 4, 7, and 10 mol%) alloys were investigated as anode materials for lithium-ion batteries. The $Al_{68}Si_{25}Ni_7$ anode showed a maximum capacity of 840 mA h g^{-1} at the fifth cycle and maintained 661 mA h g^{-1} after 40 cycles with a high coulumbic efficiency of 93%. The specific capacity increased as the decrease in the Ni content during the first 20 cycles, but the cycle performance became poorer. For the $Al_{65}Si_{25}Ni_{10}$ anode, the specific capacity increased slowly as the cycles increased and reached 370 mA h g^{-1} after 40 cycles. When the $Al_{68}Si_{25}Ni_7$ ribbons were annealed, their initial capacity became higher, but much poorer cycle performance and low coulumbic efficiency occurred. Except $Al_{65}Si_{25}Ni_{10,}$ the AlLi compound could be detected in the anodes after lithiation. However, the capacity faded rapidly due to the formation of excessive AlLi in the $Al_{73}Si_{25}Ni_2$ and annealed $Al_{68}Si_{25}Ni_7$ anodes. The experiments revealed that the as-quenched ribbons consisted of the nanoscaled α-Al, metallic glass and α-Si, and their fractions were dependent on the Ni content. The α-Al was a supersaturated solid solution of Si and Ni in fcc-Al. For the as-quenched $Al_{68}Si_{25}Ni_7$ ribbons, the α-Al grains were embedded in the amorphous matrix. It can be understood that metallic glass can store Li, and the supersaturated solid solution can store Li even more easily compared with other known Al–Si-based alloys. A conclusion can be drawn that the microstructure that the nanoscaled α-Al embedded in the metallic glass matrix is beneficial to improve the structure stability, restrain serious structural evolution, and limit the volume variation and pulverization during electrochemical cycles.

Keywords Al–Si–Ni alloys · Nanocrystal · Metallic glass · Electrochemical properties · Lithium-ion batteries

L. Zhang · X. Song · F. Wang · Q. Hu · Z. Sun (✉) · S. Yang · L. Wang · S. Sun
MOE Key Laboratory for Non-equilibrium Synthesis and Modulation of Condensed Matter, State Key Laboratory for Mechanical Behavior of Materials, Xi'an Jiaotong University, Xi'an 710049, People's Republic of China
e-mail: szb@mail.xjtu.edu.cn

L. Zhang
e-mail: zlpp@stu.xjtu.edu.cn

Introduction

Currently, lithium-ion batteries have become one of the major power sources for a variety of electronic devices. The anode material for commercial lithium-ion batteries is mainly graphite, whose low theoretical capacity (372 mA h g^{-1}) [1] has been a limiting factor in the development of high capacity. Plentiful efforts have now been taken to improve the properties of lithium-ion batteries by developing new electrode materials [2–5]. Thus, the alloy anodes, especially those that are made up of group IV B elements of Si and Sn and have higher theoretical lithium storage capacity ($Li_{4.4}Sn$, 994 mA h g^{-1}; $Li_{4.4}Si$, 4,200 mA h g^{-1}) [6, 7] have been extensively investigated as the potential anode alternatives for lithium-ion batteries. However, these electrode materials of high theoretical capacity exhibit poor cyclability. Therefore, nanoscaled anode materials are investigated extensively due to their high specific surface area and volume effect. Varieties of nanoscaled materials are fabricated as lithium-ion battery electrodes. Recently, Das et al. [8] reported that the nano-composites $SnO(V_2O_3)_{0.5}$ showed an initial capacity of 435(±5) mA h g^{-1} and stabilized to 380(±5) mA h g^{-1} with no noticeable fading in the range of 10–60 cycles. Pan et al. [9] developed NiO films as the high-energy-density lithium-ion battery anodes, which maintained a capacity of 560 mA h g^{-1} as well as capacity retention of 97% after 100 cycles at a rate of 1.0 C. When the current density was increased to 14 C, 42% of the capacity could still be retained.

Meanwhile, much attention has been paid to Al, which also has very high theoretical lithium storage capacity ($Li_{2.25}Al$, 2,235 mA h g^{-1}) [2]. However, pure Al presents much poorer cycle performance, too, and it is difficult to produce Al-based materials into nanoscale due to their active chemical properties in the air. Then, Al-based composite materials and thin film anodes are designed to improve the structure stability and electrochemical properties. For example, Lei [10] reported that the initial reversible capacities of Al–1 wt% Co_3O_4, Al–3 wt% Co_3O_4, and Al–5 wt% Co_3O_4 were 731, 697, and 656 mA h g^{-1}, and their capacity retentions were 66.8%, 69.9%, and 70.1% after ten cycles, respectively. Hu [11] reported that thin film Al–Sn alloy anodes prepared by electron-beam deposition with high Al content (Al–33 wt% Sn) delivered a relatively high initial discharge capacity of 752 mAh g^{-1}, while the electrode with high Sn content (Al–64 wt% Sn) could undergo 50 cycles life with a stable specific capacity of about 300 mA h g^{-1}.

Melt spinning is an effective method to prepare alloys with fine microstructure under the non-equilibrium state [12–14]. In our prior investigations [15–18], the melt-spun Al–Si–Mn and Al–Si–Cu ribbons were prepared as lithium-ion battery anode materials. In the investigations, nanocrystalline $Al_{67}Si_{30}Mn_3$ showed a low capacity of 326 mA h g^{-1} but a very stable cycle performance during 40 cycles, and the AlLi intermetallic compound did not appear in the lithiated Al–Si–Mn anodes [16]. Although the $Al_{71}Si_{25}Cu_4$ anode exhibited a discharge specific capacity of 1,324 mA h g^{-1} initially, its capacity was only 508 mA h g^{-1} after 20 cycles, and a great deal of AlLi intermetallic compound was detected in the lithiated alloys [18].

The lithiated mechanisms of melt-spun Al–Si–Mn and Al–Si–Cu were different [15–18]. Thus, it can be predicted that the third component has a key influence on the mechanism of the Al–Si-based anode materials. According to binary alloy phase diagrams [19], neither Mn nor Cu can form intermetallic compounds with Li, but the solubility of Li in Mn is minimum, while the solubility of Li in Cu is nearly to 20%. The phase diagram of Ni–Li is similar to that of Mn–Li, but the solubility of Li in Ni is larger at high temperature, indicating a different interaction between Li–Mn and Li–Ni. Furthermore, the radius of Ni (0.162 nm) is close to that of Cu (0.157 nm) but less than that of Mn (0.179 nm), which influences the lattice parameter of α-Al and might result in different lithiation behaviors. Therefore, adding Ni into the Al–Si alloys prepared by rapid solidification may modulate the lithiation mechanism to further improve the electrochemical properties. In this experiment, non-equilibrium $Al_{75-X}Si_{25}Ni_X$ (X=2, 4, 7, and 10 mol%) anode materials were prepared by melt-spinning for the purpose of developing new anode materials and investigating the law that the lithiated mechanism depends on the third component. The results showed that the melt-spun $Al_{68}Si_{25}Ni_7$ anode composed of nanoscaled α-Al and metallic glass exhibited high specific capacity and favorable cycle performance.

Experiment

Pure Al (99.95, wt%), pure Si (99.99, wt%), and pure Ni (99.95, wt%) were used to synthesize the Al–Si–Ni alloys. The starting materials were arc-melted employing a non-consumable tungsten electrode. The ingots were inserted into a quartz tube with a bottom hole and melted by high frequency induction. After they were overheated to the required temperature, the alloy ribbons were then prepared by single roller melt spinning under a pressure of 0.5 atm Ar gas. The ribbons obtained were 3 mm wide and 20–30 μm thick. In order to investigate the influences of phase structure, thermodynamic state, and microstructure on the electrochemical properties, some $Al_{68}Si_{25}Ni_7$ ribbons were annealed at 550 K for 2 h. The phase structures of the as-quenched and annealed ribbons were measured by a Bruker D8 advanced X-ray diffractometer (XRD) with the Cu K_α radiation at an operating voltage of 40 kV and operating current of 40 mA. The states of the as-quenched ribbons were analyzed by a Netzsch STA-449C simultaneous thermal analyzer in the temperature range from 323 to 723 K and at a heating rate of 10 K min^{-1}. The microstructures of the as-quenched and annealed ribbons were observed by a JEM-2100 transmission electron microscope (TEM) at a high accelerating voltage of 200 kV, and the foil specimens used for TEM were prepared by an ion polishing.

The as-quenched ribbons were prepared into powders by ball milling for 2 h under Ar gas protection, and then carbon black was added into the powders and mixed homogenously. Subsequently, the mixture was blended with polyvinylidene fluoride (PVDF) dissolved in *N*-methylpyrrolidinone (NMP). The ratio of the powder, carbon black, and PVDF was 84:8:8. The slurry was evenly filled in the porous Ni and dried at 373 K in a vacuum oven for 10 h to remove NMP. The electrochemical measurements were carried out in the two-electrode Swagelok cells, which were composed of alloy anode as the working electrode, a pure lithium foil as the counter electrode, Celegard 2400 as separator and 1 M LiPF6 in ethylene carbonate (EC)–diethyl carbonate (DEC) (1:1, *v*/*v*) as electrolyte. The simulation cells were assembled in a dry glove box filled with pure Ar (99.999%). The electrochemical properties of electrodes were measured by an Arbin BT-2000 instrument under a constant current density of 0.1 A g^{-1}. The low cut-off voltage of 0.03 V and the high cut-off voltage of 1 V were used in the cycles. The cyclic voltammetric measurements were measured by a VersaSTAT MC instrument at a scanning speed of 0.2 mV/s between 0 and 1 V.

The phase constitutions of the lithiated anodes were measured by the X-ray diffractometer. The morphology of the

anodes after cycling was observed by a JSM-7000F scanning electron microscope (SEM) at an accelerating voltage of 20 kV. In order to analyze the microstructural evolution during lithiation, some ribbons were directly served as the anodes, and their discharge cut-off voltage was also 0.03 V. The lithiated ribbons were prepared into TEM samples, and their microstructure was observed by TEM.

Results

Figure 1 shows the X-ray diffraction patterns of the as-quenched $Al_{75-X}Si_{25}Ni_X$ (X=2, 4, 7, 1and 0) and the annealed $Al_{68}Si_{25}Ni_7$ ribbons. The diffraction peaks of α-Al and α-Si appeared in the patterns of the as-quenched $Al_{75-X}Si_{25}Ni_X$ when X=2, 4, and 7, but the intensity of the α-Al peaks reduced as the increase of the Ni content. It is worth to be noticed that the diffraction peaks that appeared in other ribbons could not be detected clearly for $Al_{65}Si_{25}Ni_{10}$, indicating that metallic glass had evolved into the dominating composition. When the $Al_{68}Si_{25}Ni_7$ ribbons were annealed, all the diffraction peaks of α-Al and α-Si, as shown in Fig. 1, became much stronger. The other strong peaks, as denoted by the inverted triangle, appeared. It could be inferred that they belonged to one or two Al/Si/Ni compounds [20], although the types were not identified clearly. Meanwhile, the diffraction peaks that appeared in all the XRD patterns of the as-quenched ribbons were very weak, suggesting that only a few compounds were formed during rapid solidification. The XRD results implied that the lattice parameter of α-Al in the as-quenched $Al_{75-X}Si_{25}Ni_X$ (X=2, 4, and 7) ribbons was 0.4036, 0.4035, and 0.4034 nm, respectively, but it was 0.4048 nm in the annealed $Al_{68}Si_{25}Ni_7$ ribbons. It could be

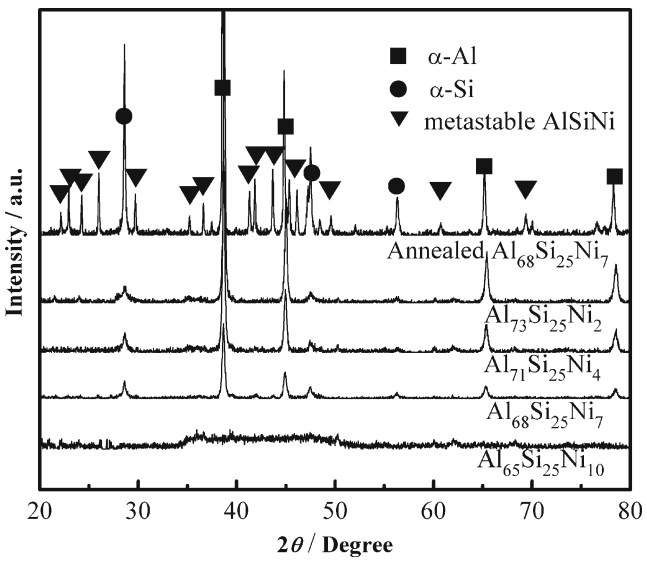

Fig. 1 X-ray diffraction patterns of the as-quenched $Al_{75-X}Si_{25}Ni_X$ (X=2, 4, 7, and 10) and annealed $Al_{68}Si_{25}Ni_7$ ribbons

concluded that α-Al in the as-quenched ribbons was a supersaturated solid solution of Si and Ni in fcc-Al and that the lattice distortion became smaller as the increase of the Ni content.

Figure 2 illustrates the microstructures of the as-quenched $Al_{75-X}Si_{25}Ni_X$ (X=2, 4, and 7) and annealed $Al_{68}Si_{25}Ni_7$ ribbons. The size of α-Al grains in the as-quenched $Al_{73}Si_{25}Ni_2$ ribbons was only <10 nm. It was noticed that the metallic glass co-existed in the ribbons, shown in Fig. 2a. The volume fraction of metallic glass, as shown in Fig. 2b, became larger as the Ni content increased to 4%. Furthermore, for the $Al_{68}Si_{25}Ni_7$ alloy, metallic glass evolved into the matrix due to an obvious increase of its volume fraction, in which nanoscaled α-Al was embedded. In the annealed $Al_{68}Si_{25}Ni_7$ alloy, however, metallic glass disappeared, and the grain size tended to coarsen.

The differential scanning calorimetry (DSC) curves of the as-quenched $Al_{75-X}Si_{25}Ni_X$ ribbons are shown in Fig. 3. The clear exothermal peaks between 400 and 450 K might indicate the crystallization of metallic glass; the other exothermal peaks should respond to the decomposing of the supersaturated solid solution and the formation of intermetallic compounds. These results confirmed that the state of the as-quenched alloys was non-equilibrium. The DSC curves (Fig. 3) indicated that the decomposing temperatures of the present non-equilibrium Al–Si–Ni alloys were lower than those of Al–Si–Mn [17] and near to those of Al–Si–Cu [18]. It could be deduced that the diffusion activation energy of the components in the melt-spun Al–Si–Ni system was lower than that in Al–Si–Mn alloys but close to that in Al–Si–Cu alloys.

Figure 4 shows the cycle properties and the coulumbic efficiency of the as-quenched $Al_{75-X}Si_{25}Ni_X$ (X=2, 4, 7, and 10) and annealed $Al_{68}Si_{25}Ni_7$ anodes. The $Al_{73}Si_{25}Ni_2$ anode exhibited an initial discharge capacity of 1,379 mA h g^{-1} but continuously faded to 350 mA h g^{-1} after 40 cycles. The $Al_{71}Si_{25}Ni_4$ anode showed a similar capacity variation tendency but lower capacity. For the $Al_{68}Si_{25}Ni_7$ anode, an initial discharge specific capacity of 727 mA h g^{-1} exhibited, and then the capacity increased to a maximum of 840 mA h g^{-1} at the fifth cycle. Subsequently, it displayed a stable cycle performance and maintained 661 mA h g^{-1} after 40 cycles. Such a result indicated that the electrochemical properties of the as-quenched Al–Si–Ni alloys with an optimum composition were improved compared with the melt-spun Al–Si–Mn anodes [15–17] and $Al_{75-X}Si_{25}Cu_X$ [18]. The initial discharge capacity of the $Al_{65}Si_{25}Ni_{10}$ anode was only 361 mA h g^{-1}. After a little initial irreversible capacity appeared, the capacity slowly increased to 374 mA h g^{-1} after 40 cycles. The coulumbic efficiency of more than 90% could be obtained in all the anodes from the as-quenched ribbons. For the anode prepared from the annealed $Al_{68}Si_{25}Ni_7$ ribbons, the capacity reached 1,372 mA h g^{-1} at the first cycle and then declined

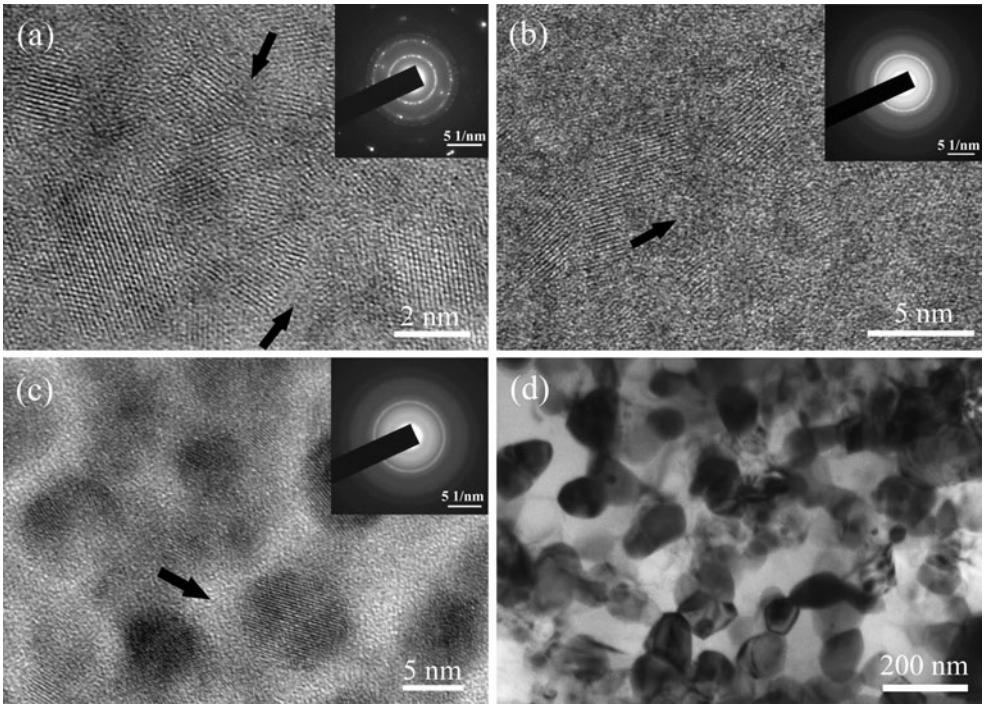

Fig. 2 Microstructures of the as-quenched $Al_{73}Si_{25}Ni_2$ (**a**), $Al_{71}Si_{25}Ni_4$ (**b**), $Al_{68}Si_{25}Ni_7$ (**c**), and annealed $Al_{68}Si_{25}Ni_7$ (**d**) ribbons. The *black arrows* denote the metallic glass

rapidly to 150 mA h g^{-1}, only experiencing 20 cycles. Meanwhile, its coulumbic efficiency reduced to 80% due to grain growth coarsening during annealing.

The X-ray diffraction patterns of the lithiated anodes are shown in Fig. 5. For the anodes prepared from the as-quenched ribbons, the strong diffraction peaks of the AlLi intermetallic compound were clearly detected in $Al_{73}Si_{25}Ni_2$, while the intensity of the AlLi peaks was much weak for $Al_{68}Si_{25}Ni_7$ and could not be detected for $Al_{65}Si_{25}Ni_{10}$. However, for the annealed $Al_{68}Si_{25}Ni_7$ anode, the intensity of AlLi diffraction peaks was the strongest. The Li–Si compounds were not found in all the lithiated anodes, and the relative peak intensities of α-Si and Al/Si/Ni compounds were not changed significantly compared with those which appeared in the patterns of the as-quenched and annealed ribbons (Fig. 1).

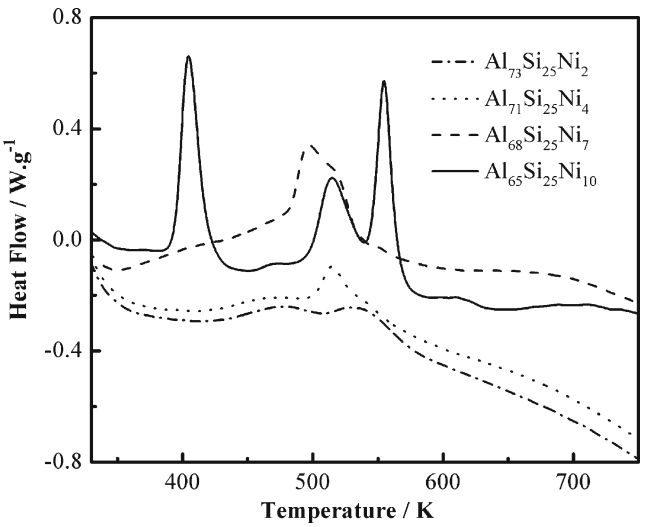

Fig. 3 Differential scanning calorimetry curves of the as-quenched $Al_{75-X}Si_{25}Ni_X$ (X=2, 4, 7, and 10) ribbons

Figure 6 displays the cyclic voltammetric curves of the as-quenched $Al_{75-X}Si_{25}Ni_X$ and annealed $Al_{68}Si_{25}Ni_7$ anodes. The cathodic current peak that appeared at about 0.55 V in the first cycle was due to a formation of the solid electrolyte interphase [21], which may lead to the initial irreversible capacity. Two current peaks were clearly measured in the $Al_{73}Si_{25}Ni_2$ and $Al_{71}Si_{25}Ni_4$ anodes, seen in Fig. 6a and b. According to the XRD results shown in Fig. 5 and [2, 11, 22], it could be concluded that the cathodic current peaks appeared at near 0.12 V due to the formation of AlLi, while the anodic peaks appeared at 0.62 V because of its decomposition. The current peaks, as shown in Fig. 6a–d, became flatter as the increase in the Ni content in the present work. For the $Al_{65}Si_{25}Ni_{10}$ anode, the cathodic peak disappeared, and the anodic peaks became broader and weaker. However, for the annealed $Al_{68}Si_{25}Ni_7$ anode, the sharp current peaks were displayed again, as can be seen in Fig. 6e. It could be concluded that not only does the alloy composition influence the lithiation mechanism but also the effect of the thermodynamic state on the mechanism is very evident. Besides, the lithiation of α-Si and Al/Si/Ni compounds did not clearly occur in the present investigation.

The images of the microstructure and electron diffraction pattern of the lithiated $Al_{73}Si_{25}Ni_2$ alloys are shown in

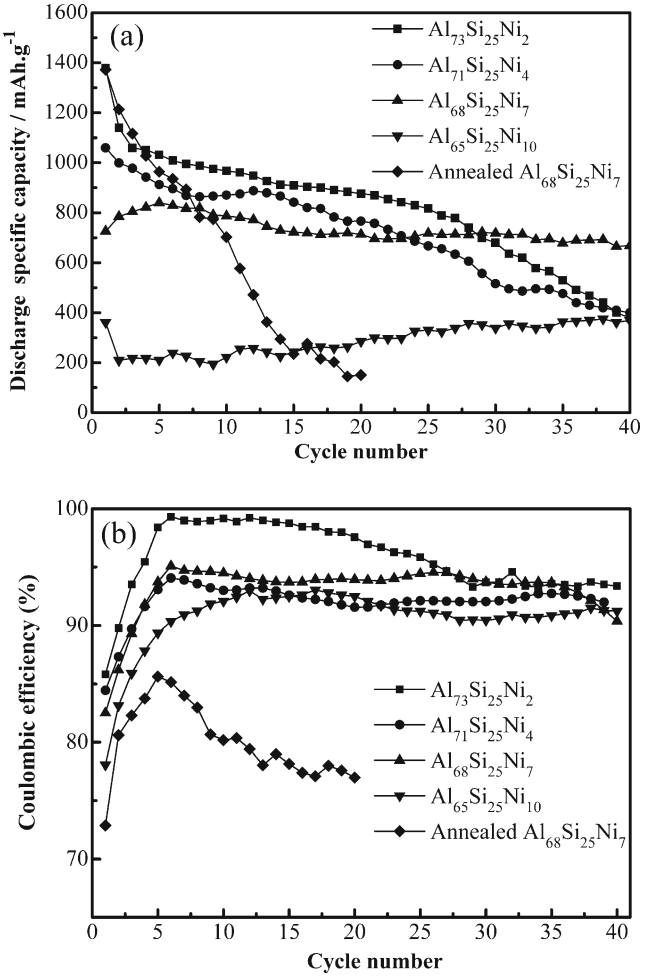

Fig. 4 Cycle performance (**a**) and coulombic efficiency (**b**) of the as-quenched $Al_{75-X}Si_{25}Ni_X$ and annealed $Al_{68}Si_{25}Ni_7$ anodes

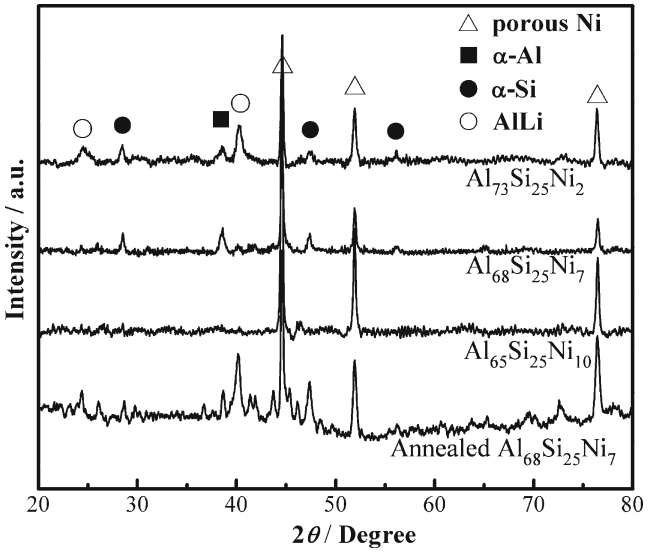

Fig. 5 X-ray diffraction patterns of the lithiated anodes prepared from the as-quenched $Al_{75-X}Si_{25}Ni_X$ (X=2, 7, and 10) and annealed $Al_{68}Si_{25}Ni_7$ ribbons

Fig. 7. The indication of crystallization of metallic glass could not be clearly observed. However, the electron diffraction pattern and high resolution images confirmed the appearance of an AlLi intermetallic compound. The AlLi grains were nanoscaled, but some α-Al grains could still be observed, which resulted in the co-existence of AlLi, α-Al, and metallic glass.

Figure 8 shows the SEM images of the $Al_{75-X}Si_{25}Ni_X$ anodes from the as-quenched alloy powders and the annealed $Al_{68}Si_{25}Ni_7$ anode after cycling. For the lithiated $Al_{73}Si_{25}Ni_2$ anode, a lot of bulges appeared in the powder surfaces, suggesting their relation to the volume explosion caused by the formation of AlLi. Some cracks and exfoliation could be observed, as shown in Fig. 8a. For the $Al_{71}Si_{25}Ni_4$ anode, cracks could still be observed, but the bulges disappeared. A slight exfoliation still existed, as can be seen in Fig. 8b. When the Ni content was 7%, the cracks became fewer, and the obvious indication of exfoliation disappeared, as shown in Fig. 8c. There were no obvious cracks in the $Al_{65}Si_{25}Ni_{10}$ anode, as can be seen in Fig. 8d. For the annealed $Al_{68}Si_{25}Ni_7$ anode, serious pulverization was observed, as shown in Fig. 8e. These results indicated that pulverization, exfoliation, and cracks responded to capacity fade in the present investigation.

Discussion

When the Ni content was 2% and 4%, the anodes performed high initial capacities and fast capacity fade. For the as-quenched $Al_{68}Si_{25}Ni_7$ anode, a maximum capacity of 840 mA h g^{-1} was exhibited, and a capacity of 661 mA h g^{-1} was maintained after 40 cycles. These results meant that the initial capacities decreased, and the cycle performance became more stable as the Ni content increased. When the Ni content increased to 10%, the anode exhibited a continuous increasing tendency of capacity. After lithiation, an intermetallic compound of AlLi could be measured in the as-quenched $Al_{75-X}Si_{25}Ni_X$ (X=2, 4, and 7) anodes, and the quantity of the AlLi compound reduced as the increase in the Ni content (Figs. 5, 6, and 7). For the annealed $Al_{68}Si_{25}Ni_7$ alloy, the initial specific capacity was large, but the capacity fade was rapid in the following cycles. The strongest AlLi diffraction peaks, sharp current peaks, and serious pulverization appeared during the cycles (Figs. 5, 6, and 8). The as-quenched $Al_{75-X}Si_{25}Ni_X$ (X=2, 4, 7) ribbons were non-equilibrium in thermodynamics and consisted of nanoscaled supersaturated α-Al, metallic glass, and α-Si. The fraction of metallic glass increased with the Ni content (Figs. 1, 2, and 3). It can be inferred that the optimum composition, special microstructure, and non-equilibrium state in

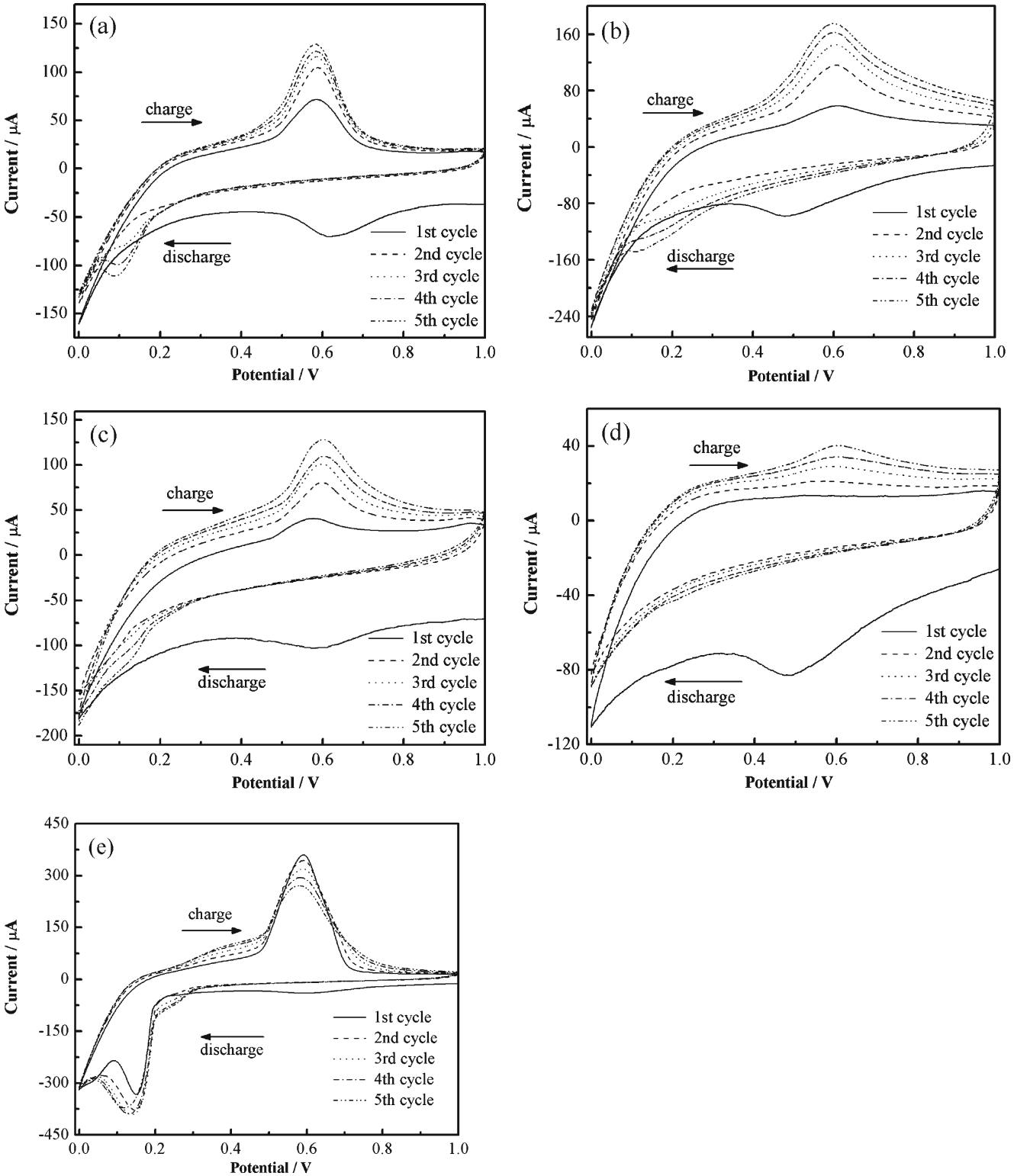

Fig. 6 Cyclic voltammetric curves for the as-quenched $Al_{73}Si_{25}Ni_2$ (**a**), $Al_{71}Si_{25}Ni_4$ (**b**), $Al_{68}Si_{25}Ni_7$ (**c**), $Al_{65}Si_{25}Ni_{10}$ (**d**), and annealed $Al_{68}Si_{25}Ni_7$ (**e**) anodes

thermodynamics are the key factors to achieve favorable electrochemical properties and affect the lithiation mechanism of the Al–Si–Ni alloys.

For the as-quenched $Al_{65}Si_{25}Ni_{10}$ ribbons, the metallic glass became the dominating composition (Fig. 1). The anode exhibited a capacity of more than 200 mA h g^{-1}

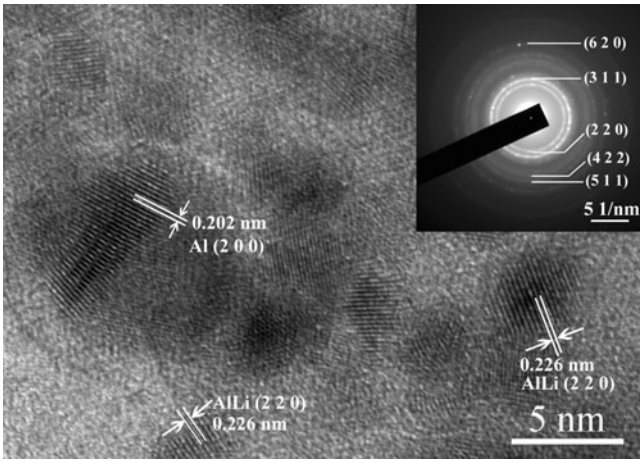

Fig. 7 Microstructure of the lithiated as-quenched $Al_{73}Si_{25}Ni_2$ alloy

(Fig. 4), and the formation of AlLi did not occur (Figs. 5 and 6d). It can be concluded that the metallic glass can store Li atoms relying on solution. This reveals another fact that Li atoms can diffuse in the metallic glass. During lithiation of metallic glass, Li atoms have to substitute some atomic sites of the parent alloys, and its density will decrease after Li atoms are extracted. The sites employed for Li storage in the alloys increase as the alloys experience several cycles, which explains the continuous capacity increase for $Al_{65}Si_{25}Ni_{10}$ over 40 cycles and $Al_{68}Si_{25}Ni_7$ at the first few cycles in the present work. Besides, the atom arrangement of the metallic glass is usually loose, and the activation energy is lower compared with that of crystals. As a result, the diffusion coefficient is relatively high [23].

Only a small quantity of α-Si existed in the as-quenched Al–Si–Ni alloys, and it was embedded in the metallic glass or supersaturated solid solution. α-Si was not alloyed by Li during the discharge/charge processes (Figs. 5 and 6), which is consistent with the Al–Si–Mn [15–17] and Al-Si-Cu systems[18]. Both metallic glass and the Al-based supersaturated solid solution consisted of three components, so the thermodynamic condition of the co-existence of α-Al and AlLi during lithiation was met. The DSC curves of the Al–Si–Ni system (Fig. 3) indicate that their separating temperatures

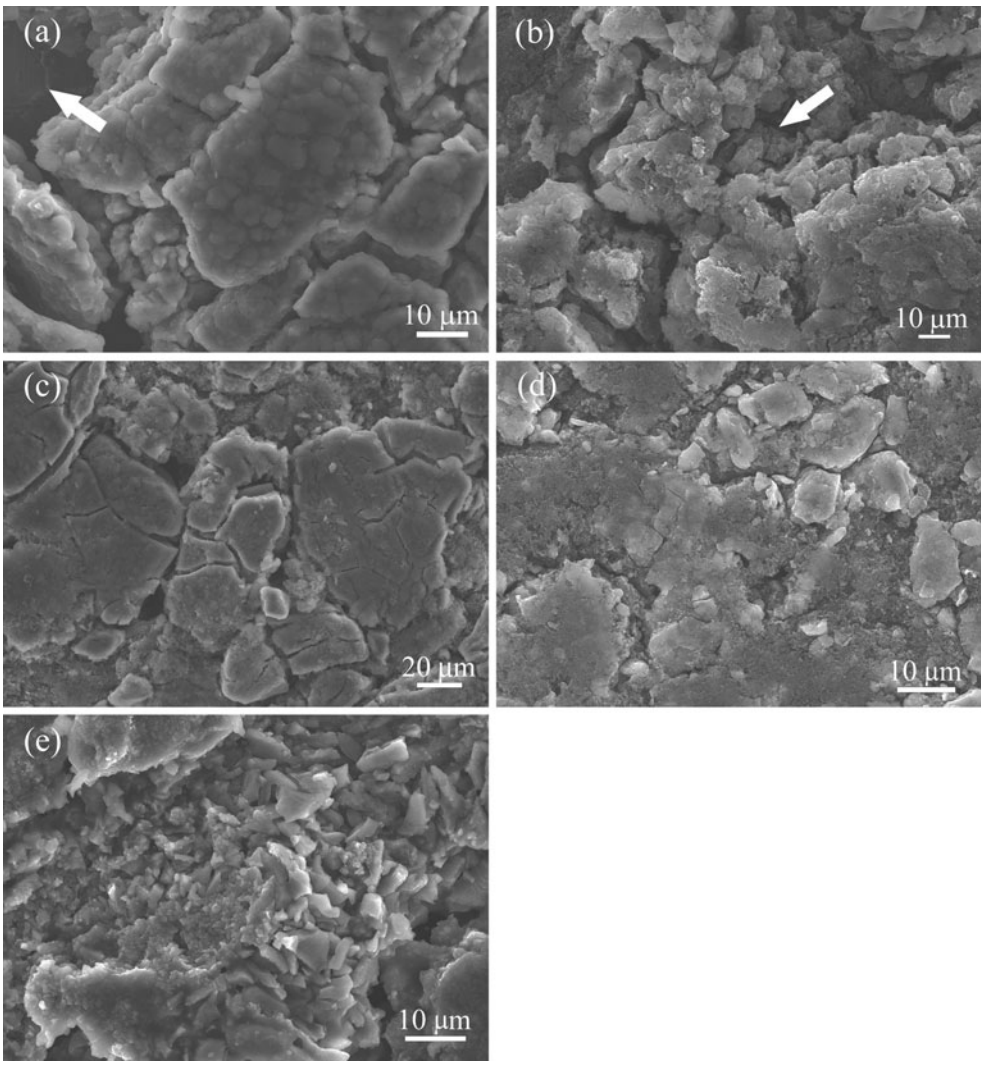

Fig. 8 Morphology of the lithiated $Al_{73}Si_{25}Ni_2$ (**a**), $Al_{71}Si_{25}Ni_4$ (**b**), $Al_{68}Si_{25}Ni_7$ (**c**), $Al_{65}Si_{25}Ni_{10}$ (**d**), and annealed $Al_{68}Si_{25}Ni_7$ (**e**) anodes after cycling. The *arrows* denote the exfoliation of the alloy powders

were lower than those of Al–Si–Mn [16]. It means that the diffusion activation energy of atoms in the present non-equilibrium Al–Si–Ni alloys is lower than that in Al–Si–Mn [16], resulting in the easier formation of AlLi in the present alloys during lithiation. The difference of atomic radiuses may be an important factor that influences the lithiation mechanism. The radius of Al, Ni, Cu, Mn, and Li is 0.182, 0.162, 0.157, 0.179, and 0.205 nm, respectively. For the Al–Si-based supersaturated solid solution, the lattice parameter of α-Al around Ni atoms decreases much more than that around Mn which changes a little [15]. The decrease is beneficial to the storage of Li with a larger atom radius, leading to higher capacity. Generally, the formation of an intermetallic compound must meet the conditions of composition and structure, which are usually affected by the diffusion of several atoms. When the Li atoms were inserted into the Al–Si–Ni anodes, AlLi was relatively easy to form in the systems due to the lower diffusion activation energy of atoms (Fig. 3). The result is similar to that of the melt-spun Al–Si–Cu anodes [18], but much different from that of Al–Si–Mn [17]. Although the formation of AlLi causes structure evolution, pulverization and rapid capacity fade do not occur in the anodes from the as-quenched ribbons. The reason is that the metallic glass matrix can improve the structure stability and limit the volume variation. At the same time, the evolution that appeared in the nonoscaled α-Al grains only resulted in a little absolute volume variation. The volume fraction of metallic glass in the $Al_{73}Si_{25}Ni_2$ and $Al_{71}Si_{25}Ni_4$ ribbons was a little, so the volume variation caused by the formation of AlLi could not be very effectively restricted, which led to poorer cycle performance (Fig. 4). While for the $Al_{68}Si_{25}Ni_7$ alloy, a small quantity of AlLi formed (Figs. 5 and 6c), and the volume variation was effectively mitigated (Fig. 8c) by the metallic glass matrix (Fig. 2c). In addition, the grain size in the as-quenched alloys was nanoscaled (Fig. 2). As the fraction of the interface between the grains and metallic glass increases greatly, much more Li can be stored in the interface of the as-quenched alloys. The increase in surface tension will also increase the solubility of Li in α-Al and metallic glass. As a result, a favorable property was achieved in the as-quenched $Al_{68}Si_{25}Ni_7$ alloy. However, Ni in the alloys is inert for lithiation. Its content not only controls the microstructure but also influences the Li storage ability of the supersaturated solid solution and metallic glass. When the Ni content is excess, the Li storage ability of the alloys will be weaken, resulting in a lower capacity and a better cycle performance ($Al_{68}Si_{25}Ni_7$ and $Al_{65}Si_{25}Ni_{10}$).

After the $Al_{68}Si_{25}Ni_7$ alloy was annealed, the metallic glass crystallized. α-Al evolved into the matrix while the grain size tended to coarsen (Figs. 1 and 2). A great amount of AlLi compound formed in after lithiation (Fig. 5), and the restrictive effect of metallic glass on volume variation was lost. Although the Li storage ability of the Al/Si/Ni compounds has not been identified, it is very clear that the excess volume variation, which is manifested by large initial capacity, together with non-stable structure has caused the serious pulverization. As a result, capacity faded rapidly (Fig. 4). It could be concluded that the non-equilibrium state is very beneficial to the improvement of electrochemical properties.

For the as-quenched Al–Si–Mn [15, 16] anodes, the structure evolution was not clearly detected, resulting in lower capacity and stable cyclability. On the contrary, a lot of AlLi compound formed in the as-quenched Al–Si–Cu [18]. The capacity was large initially, but then faded gradually. In the present system, the structure evolution caused by the formation of AlLi was restricted by the metallic glass matrix, which led to higher capacity and more stable cycle performance, especially for $Al_{68}Si_{25}Ni_7$. All the results reveal that the effects of the third component on the lithiation mechanism and electrochemical properties are obvious for the Al–Si-based alloys. Anode materials owning favorable properties could be obtained by skillful adoption of transition metal elements as the third component and by careful control of their concentration.

Conclusions

Melt-spun $Al_{75-X}Si_{25}Ni_X$ (X=2, 4, 7, and 10 mol%) ribbons were metastable and consisted of nanograins of the supersaturated solid solution α-Al, metallic glass, and α-Si. The fraction of metallic glass became larger as the increase in the Ni content. The $Al_{73}Si_{25}Ni_2$ and $Al_{71}Si_{25}Ni_4$ anodes exhibited high initial capacity, but their capacity gradually faded as the cycles increased. For the $Al_{68}Si_{25}Ni_7$ anode, a more stable cycle performance was achieved, and a maximum capacity among the present $Al_{75-X}Si_{25}Ni_X$ anodes appeared after 30 cycles. As the alloy anode was mainly composed of metallic glass ($Al_{65}Si_{25}Ni_{10}$), it performed a continuous increase of capacity over 40 cycles. The high coulumbic efficiency of more than 90% could be obtained in all the anodes from the as-quenched ribbons. Except the $Al_{65}Si_{25}Ni_{10}$ anode, the AlLi intermetallic compound could be detected after lithiation. It can be confirmed that the metallic glass can store Li atoms and provide rapid diffusion medium. Numerous Li atoms were stored in the supersaturated α-Al, and plenty of interfaces between metallic glass and nanograins contributed a lot to capacity. It is concluded that the microstructure of the nanoscaled α-Al embedded in the metallic glass matrix could improve the structure stability, restrain serious structural evolution, and limit the volume variation and pulverization. After the $Al_{68}Si_{25}Ni_7$ alloy was annealed, the rapid capacity fade and coulumbic efficiency decrease occurred, resulting from the crystallization of metallic glass, supersaturated solid solution decomposition, and grain coarsening.

Acknowledgements This work was supported by the National Natural Science Foundation of China (50871081, 51002117, and 51071117).

References

1. Menachem C, Peled E, Burstein L, Rosenberg Y (1997) J Power Sources 68:277–282
2. Hamon Y, Brousse T, Joousse F (2001) J Power Sources 97–98:185–187
3. Beaulieu LY, Hatchard TD, Bonakdarpour A, Fleischauer MD, Dahn JR (2003) Electrochem Soc 150(11):A1457–A1464
4. Obrovac MN, Christensen L (2004) Electrochem Solid-State Lett 7 (5):A93–A96
5. Winter M, Besenhard JO (1999) Electrochim Acta 45(1–2):31–50
6. Winter M, Besenhard JO, Spahr ME, Novak P (1998) Adv Mater 10:725–763
7. Tamura N, Fujimoto M, Kamino M, Fujitani S (2004) Electrochim Acta 49:1949–1956
8. Das B, Reddy MV, Rao Subba GV, Chowdari BVR (2011) J Solid State Electrochem 15:259–326
9. Pan QM, Liu J (2009) J Solid State Electrochem 13:1591–1597
10. Lei XF, Ma JX (2009) Mater Chem Phys 116:383–387
11. Hu RZ, Zeng MQ, Li CYV, Zhu M (2009) J Power Sources 188:268–273
12. Sun ZB, Guo J, Song XP, Zhu YM, Li Y (2008) J Alloys Compd 455:243–248
13. Zhang YH, Li BW, Ren HP, Guo SH (2009) Mater Chem Phys 115:328–333
14. Yang S, Song XP, Liu XS, Li SD (2003) J Appl Phys 93:1199–1202
15. Sun ZB, Wang XD (2008) J Power Sources 182:353–358
16. Sun ZB, Li XP (2009) Sci China Ser E 52:2288–2294
17. Li Q, Hu Q, Sun ZB, Li XP (2010) Chinese J Nonferrous Metals 20:1998–2010
18. Zhang LP, Wang F, Liang P, Sun ZB (2011) Mater Chem Phys 129:1006–1010
19. Okamoto H (2000) M phase diagrams for binary alloys, Li–Cu P 300, Li–Mn P 527, Li–Ni P 529. ASM International, Materials Park
20. Raghavan V (2005) J Phase Equilib Diffus 26:262–267
21. Zheng MS, Dong QF, Cai HQ, Jin MG, Lin ZG, Sun SG (2005) J Electrochem Soc 152:2207–2210
22. Chen ZX, Qian JF, Ai XP (2009) Electrochim Acta 54:4118–4122
23. Kittel C (2005) Introduction to solid state physics. Wiley, New York, p 578

Research highlights

•Melt-spinning was used to prepare Al–Si–Ni alloys composed of nanocrystal and metallic glass.
•The Al–Si–Ni alloys exhibited high reversible specific capacity and excellent cycle capability.
•AlLi compound formed in the lithiated Al–Si–Ni alloys.
•Structure evolution and volume variation could be restrained due to the metallic glass matrix.